Ain Shams Engineering Journal 16 (2025) 103399

Contents lists available at ScienceDirect

Ain Shams Engineering Journal

journal homepage: www.sciencedirect.com

Cylindrical protuberance's effect on supersonic jet's flow control: Unveiling protuberance penetration and position on jet deflection through comprehensive turbulence simulation

Mohammad Hojaji [a,b], Mohammad Eydizadeh [a], Mohammadreza Soufivand [c], Annunziata D'Orazio [c], Sayed Ali Hosseini [f], Arash Karimipour [a,*], Aliakbar Karimipour [d,e,*]

[a] *Department of Mechanical Engineering, Na.C., Islamic Azad University, Najafabad, Iran*
[b] *Aerospace and Energy Conversion Research Center, Na.C., Islamic Azad University, Najafabad, Iran*
[c] *Dipartimento di Ingegneria Astronautica, Elettrica ed Energetica, Sapienza University of Rome, Via Eudossiana 18, Roma 00184, Italy*
[d] *Institute of Research and Development, Duy Tan University, Da Nang, Vietnam*
[e] *School of Engineering & Technology, Duy Tan University, Da Nang, Vietnam*
[f] *School of Mechanical Engineering, Shiraz University, Shiraz 71348-51154, Iran*

ARTICLE INFO

Keywords:
Flow Control
Supersonic Convergent-Divergent Nozzle
Shock Waves
Shock-wave/boundary-layer interaction

ABSTRACT

Thrust vector control (TVC) through exhaust gas deflection is crucial for enhancing maneuverability, especially when aerodynamic control surfaces are ineffective. This study numerically investigates the influence of a cylindrical protuberance on the thrust vectoring of a supersonic jet as a passive, efficient TVC method. The effects of Nozzle Pressure Ratio (NPR), protuberance position, and penetration ratio on the nozzle exit flow, shock structure, and thrust deflection angle are analyzed. A convergent-divergent (C-D) nozzle is designed for a nominal Mach number of 2, and the three-dimensional, steady, compressible Navier-Stokes equations are solved using the SST k-ω turbulence model. Results reveal that protuberance-induced shocks and shock-wave/boundary-layer interaction significantly alter the flow structure and thrust deviation. The optimal protuberance position is found at 90 % of the divergent section length ($X_p/L = 0.9$), where increasing the penetration ratio (H/D^*) up to 0.22 yields a maximum thrust deflection angle of 8.1°. Additionally, higher penetration ratios generate stronger vortical structures, which, at $H/D^* = 0.2$, become more prominent and susceptible to downstream jet-fin interactions. The thrust vector deflection exhibits a near-linear relationship with the penetration ratio, with thrust losses reaching up to 6.5 % at maximum penetration. These findings provide valuable insights into shock-vector control mechanisms, offering a benchmark for future aerospace propulsion studies and enabling the development of advanced TVC systems for high-speed applications.

1. Introduction

Thrust Vector Control (TVC) is one of the most advanced techniques for controlling a flying vehicle. TVC acts by directing the exhausted main flow of an engine to provide an appropriate thrust direction [1]. As shown in Fig. 1, this technique can create rolling, pitching, and yawing moments in all flow regimes for any flying object using a flow jet [2,3]. Given its practical applications, researchers have shown significant interest in this technique. The evolution of this method has led to the widespread adoption of TVC by numerous aerial vehicles, enhancing their overall performance and maneuverability.

Generally, there are two approaches for thrust vectoring: Mechanical Thrust Vectoring Control (MTVC) and Fluidic Thrust Vectoring Control (FTVC) [3]. The following Fig. 2 presents a general classification of standard methods.

In summary, FTVC has been studied since the 1950 s, using secondary flow injection in rocket propulsion systems[4–10]. In this technique, a secondary fluid is injected into the divergent part of the nozzle. It causes a bow shock upstream, which is decisive in causing thrust vector deviation [7–15]. Despite the advantages of FTVC, erosion of hot gas transfer pipes for secondary injection (due to corrosion and high temperature of combustion gases) is the main disadvantage of this mechanism. Wu et al. (2021) investigated a numerical study of fluidic TVC using a dual throat nozzle in a 3-D state. This research examined the

---

[*] Corresponding authors: Institute of Research and Technology, Duy Tan University, Da Nang, Vietnam (Aliakbar Karimipour).
E-mail addresses: arash.karimipour@iau.ac.ir (A. Karimipour), aliakbarkarimipour@duytan.edu.vn (A. Karimipour).

https://doi.org/10.1016/j.asej.2025.103399
Received 19 December 2024; Received in revised form 4 March 2025; Accepted 28 March 2025

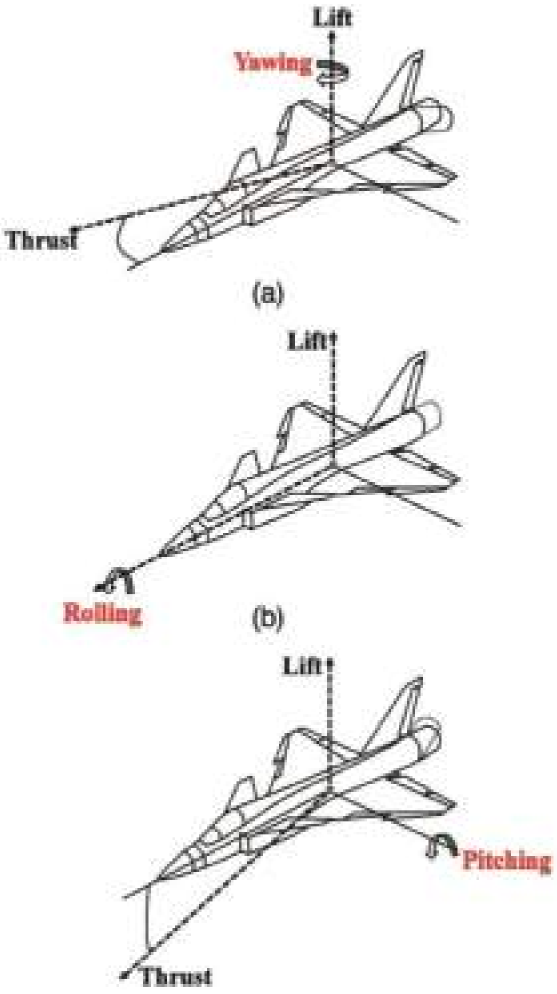

Fig. 1. Rolling, pitching, and yawing maneuvers of aircraft [2].

effects of the Nozzle Pressure Ratio (NPR), injection-to-mainstream momentum flux ratio, and setup angle of the slot injector on the systemic performance. The result shows that pitching angles decline along with an increasing NPR [16].

In 2022 and 2023, Zigunov et al. [17,18] conducted an experimental investigation into the thrust vectoring of an overexpanded circular supersonic jet using a 64-microjet-in-crossflow actuator array. A genetic algorithm was utilized to optimize the thrust vectoring angle, evaluating 900 actuator configurations. The study achieved a maximum vectoring angle of 2 degrees with azimuthal control over the vectoring direction. Results revealed an asymmetric shock structure in the nozzle's diverging section, enabling shock vector control. The same experimental setup was also applied to noise reduction in cold and hot supersonic jets, employing active flow control guided by a genetic algorithm. The findings demonstrated noise reductions of 7.3 dB for a cold overexpanded nozzle and 4.7 dB under hot conditions.

In 2025, using machine learning, Homin Kim et al. [19] optimized a dual-throat bent nozzle (DTBN) for thrust vectoring. A compressible flow analysis with the SST k-ω model evaluated 600 DTBN geometries by varying convergence angle, divergence angle, and cavity length. Random forest regression achieved the best performance among tested algorithms, accurately predicting thrust characteristics. Three optimized designs were proposed to maximize thrust magnitude, vectoring angle, and their combination. The study highlights machine learning's potential in nozzle optimization but excludes factors like nozzle inlet/exit diameters and bent angle. Future work will incorporate these parameters and validate results experimentally, advancing hybrid thrust vectoring nozzle development.

In 2025, Hosseini et al. [20] investigated the impact of secondary flow injection on TVC in beveled nozzles with 25°, 45°, and 65° bevel angles using experimental and numerical methods. Additively manufactured nozzles were tested on a high-precision two-component force balance, measuring axial and side forces. Pressure distribution was analyzed, and Rainbow-Schlieren photography visualized shock structures. At a maximum mass flow rate ratio of 8.51 %, secondary injection at 80 % of the diverging section in the 65° nozzle achieved a 19° thrust deflection. The 45° nozzle exhibited a 5 % higher specific impulse coefficient. Numerical simulations using the SST k-ω model provided more profound insights into flow interactions, complementing experimental findings on nozzle performance.

The MTVC includes revolving jet tabs, jet vane control, and movable nozzle control methods.[21–27] Among the mechanical techniques, using a tab at the nozzle exit has received more attention due to its relatively simple design and temporary presence inflow. In this

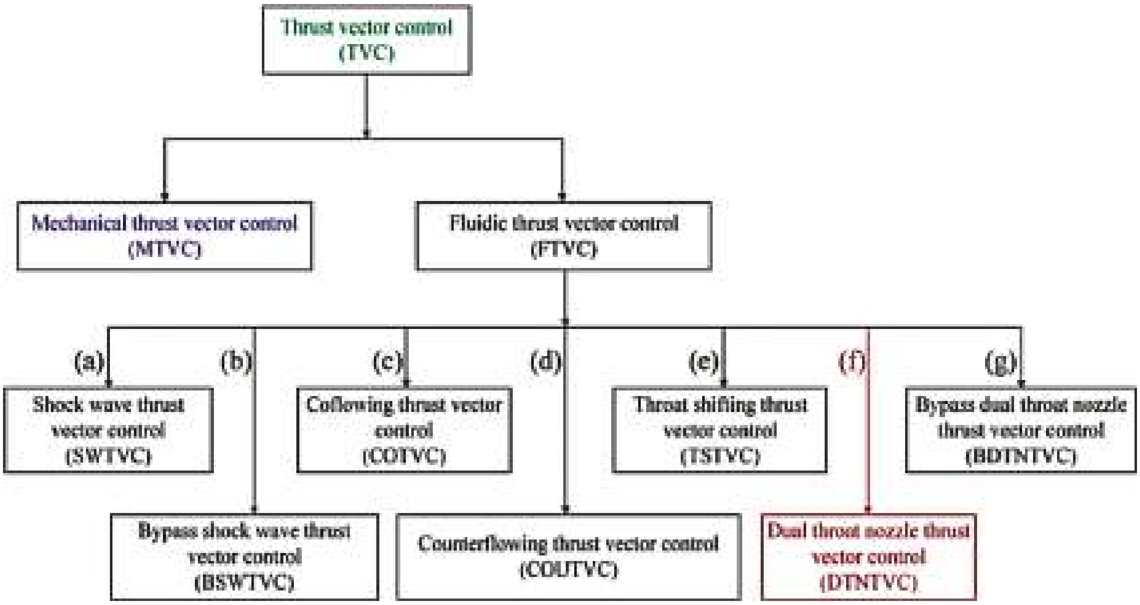

Fig. 2. Classification of the TVC methods.

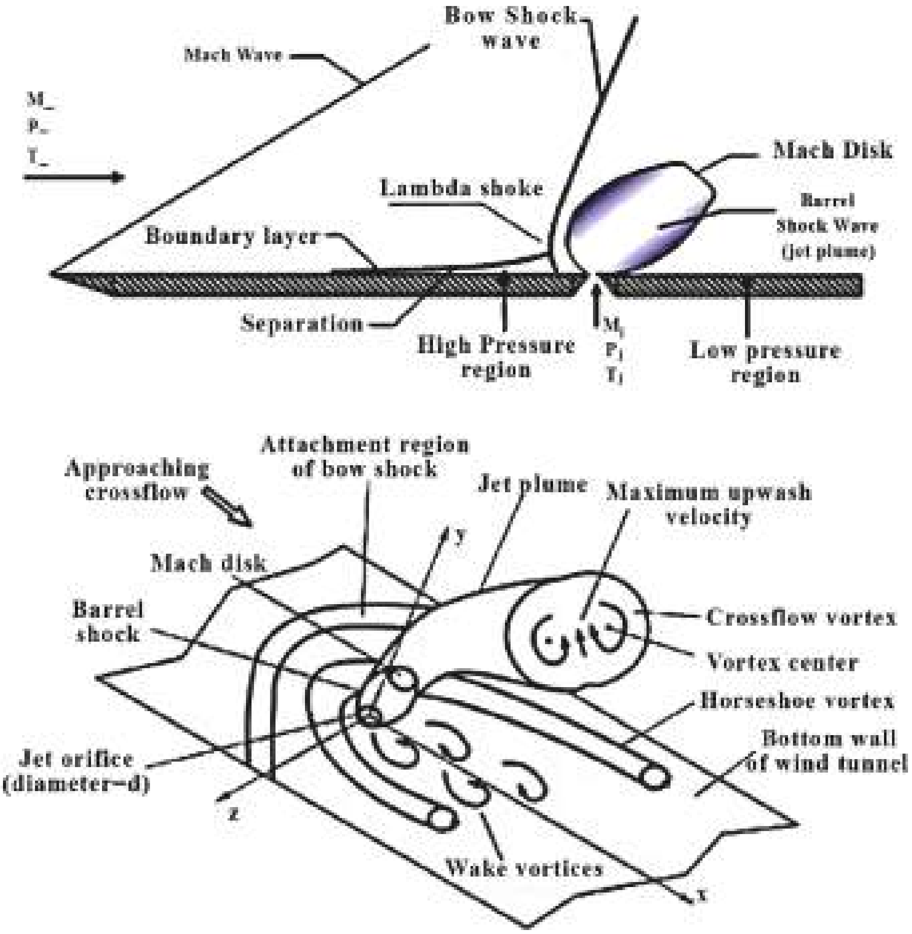

Fig. 3. A schematic of physical phenomena of the secondary injection in a supersonic flow [43,44].

technique, the tab at the nozzle outlet creates shockwaves upstream of the tab, which eventually causes the flow to deflect. This method has the disadvantage of increasing noise at the nozzle outlet. In this regard, Using waveform tabs for TVC was investigated by Phanindra et al. in 2010 [28]. The results showed that alternating plain tabs with waveform tabs reduced the length of shock trains and noises. Another limitation of this technique is the effects of thermal loads on the tab exposed to the hot gases exiting the nozzle [29]. The MTVC technique also has a general deficiency: a large number of mechanical pieces can result in overweight, overcomplicated structures [30].

Mokhtari et al. presented 2019 a new method of TVC based on an understanding of secondary fluid injection techniques [31–33]. This method used an obstacle to create a flow shock instead of a fluid injection. This idea avoids the complexities associated with fluid injection. They examined the effect of a cylindrical protuberance on the thrust vector of a C-D nozzle with a nominal Mach number of 2. It was found that the axial thrust loss and thrust vector angle were highly dependent on the location of the protuberance and its penetration ratio. Also, Babaeyan et al [34,35]. Two protuberances were used in different installation positions to control the thrust vector. Later, Thillaikumar et al. investigated the effect of struts deployed at different positions in the divergent portion of a supersonic nozzle at various expanded states on exhaust gas deflection. Their results suggest that the most efficient TVC can be achieved at over-expanded conditions with an optimal jet deflection of 3.6 degrees at a settling chamber pressure of 4 bar [36]. Also, in 2021, Li et al. conducted a numerical study on TVC using a rod in two-dime[37]nsional mode. The results showed two practical factors for TVC. The first is the location of the rod, and the other is the rod's penetration. As the penetration of the rod increases, the deflection increases, but the thrust coefficient decreases. Also, as the location of the rod is closer to the nozzle outlet, the deviation angle and the thrust coefficient increase [38].

Soufivand [39], [37] investigated TVC using shock wave manipulation and the Coanda effect in sonic flows. Numerical and experimental analyses examined the effects of protuberance location, penetration depth, and NPR on thrust vectoring. Results showed that protuberance placement significantly influenced shock structures and flow separation while increased penetration depth (up to 10 %) stabilized flow deviation.

Studies indicate that the complex physics of this flow has limited research on its simulation in the supersonic regime, leaving its underlying mechanisms largely unexplored. To address this, numerical simulations are essential for understanding intricate flow behavior and the effects of protuberance penetration on system performance. This study investigates the TVC physics in a C-D nozzle under supersonic conditions, focusing on how protuberance penetration influences thrust vector deflection. The impact of NPR, penetration ratio, and protuberance position is analyzed through comparative numerical simulations to provide deeper insights into thrust vectoring mechanisms.

1.1. *Flow physics of shock vector control approach*

In most fluid control methods, thrust vectoring is achieved by manipulating shocks generated within the nozzle, a technique known as shock vector control. This is typically accomplished through secondary fluid injection or protuberances, which act as flow obstructions, inducing shock formations such as lambda and bow shocks. These shocks arise due to the interaction of supersonic flow with obstacles,

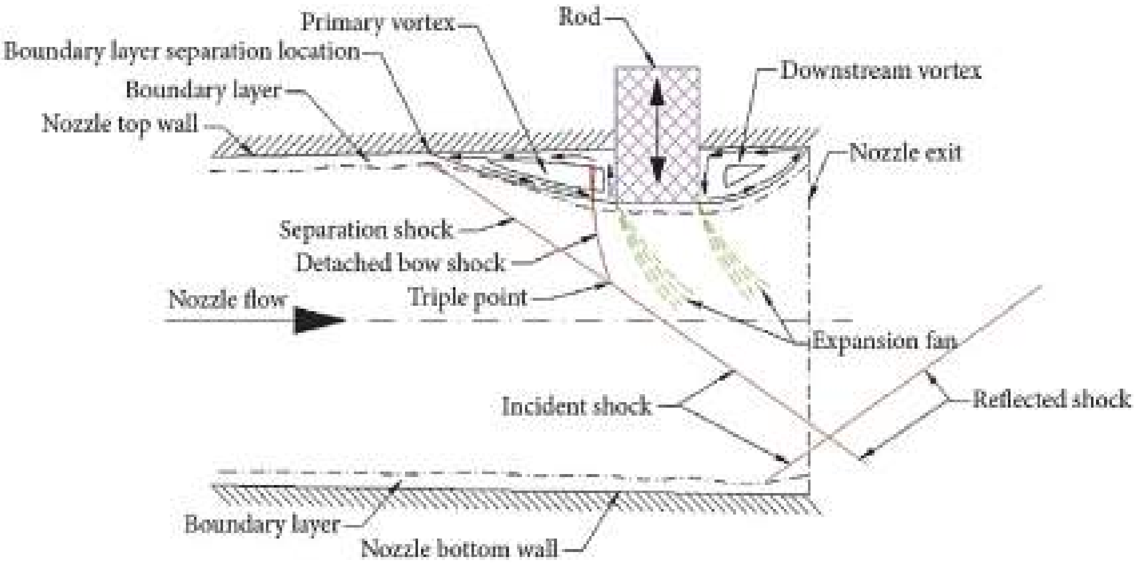

Fig. 4. Bow shock and flow deflection angle in the nozzle due to the presence of a protuberance [45].

leading to substantial changes in static pressure along the nozzle walls. The resulting pressure distribution generates lateral forces, contributing to thrust vectoring. Additionally, shock-induced flow deflection alters the thrust angle, further enhancing control over the nozzle's output direction. [40].

The concept of using a protuberance originates from secondary fluid injection, where the injected fluid behaves like a solid obstacle within the flow. In contrast, the protuberance method directly employs a solid body to generate shocks, simplifying the application. While fluid injection requires precise control of flow rates and directions, along with valves, connections, and complex mechanisms—leading to higher maintenance costs and wear over time—the protuberance approach eliminates these drawbacks. Despite this difference in implementation, the underlying flow physics and associated phenomena remain fundamentally consistent between the two methods. [31].

Fig. 3 schematically illustrates the flow field resulting from jet injection into a supersonic stream. The injection generates a separation shock upstream of the injection point, causing the boundary layer to detach from the wall. A bow shock forms in the main flow due to the injected jet acting as the primary deflection force. The interaction of weak separation shocks with strong bow shocks induces flow deflection. A rotational recirculation region develops between the separated surface and boundary layer, containing vortices that generate lambda shocks, shifting the bow shock upstream. As the injected jet interacts with the main flow, counter-rotating vortices and horseshoe-shaped vortices form, driven by pressure forces from the jet. However, this phenomenon is not observed in the protuberance method. Downstream of the injection, strong vortex motions influence the low-pressure region, further affecting flow behavior.[41,42].

In the protuberance method, similar flow physics and phenomena occur. The protuberance, positioned near the nozzle exit in the main flow path, disrupts the boundary layer, causing flow separation and the formation of shocks. These shocks, in turn, deflect the flow. As illustrated in Fig. 4, the protuberance acts as an obstacle in the supersonic stream, significantly altering the trajectory of the supersonic jet and influencing thrust vectoring.

2. Numerical Methodology

2.1. Governing equations

The study employs three-dimensional, compressible, Reynolds-Averaged Navier-Stokes (RANS) equations in steady form to simulate the flow field. The SST k-ω turbulence model, incorporating compressibility effects, is used for turbulence modeling. The finite volume method is applied, utilizing the Roe flux splitting scheme and a central difference approach to estimate diffusion fluxes through a second-order implicit method. Air is treated as an ideal gas for all computations. The general equation forms are presented in Equations (1) to (9) [13]. Given that heat generation, buoyancy forces, and gravity effects are disregarded, the right-hand side of Equation (1), denoted as J, exclusively represents the source terms related to turbulence equations [15,46]:

$$\frac{\partial U}{\partial t}+\frac{\partial F}{\partial x}+\frac{\partial G}{\partial y}+\frac{\partial H}{\partial z}=J \tag{1}$$

where,

$$U=\begin{bmatrix}\rho\\ \rho u\\ \rho v\\ \rho w\\ \rho\left(e+\dfrac{V^2}{2}\right)\end{bmatrix} \tag{2}$$

$$F=\begin{bmatrix}\rho u\\ \rho uu+P-\tau_{xx}\\ \rho vu-\tau_{xy}\\ \rho wu-\tau_{xz}\\ u\left[\rho\left(e+\dfrac{V^2}{2}\right)+P\right]-u\tau_{xx}-v\tau_{xy}-w\tau_{xz}-q_x\end{bmatrix} \tag{3}$$

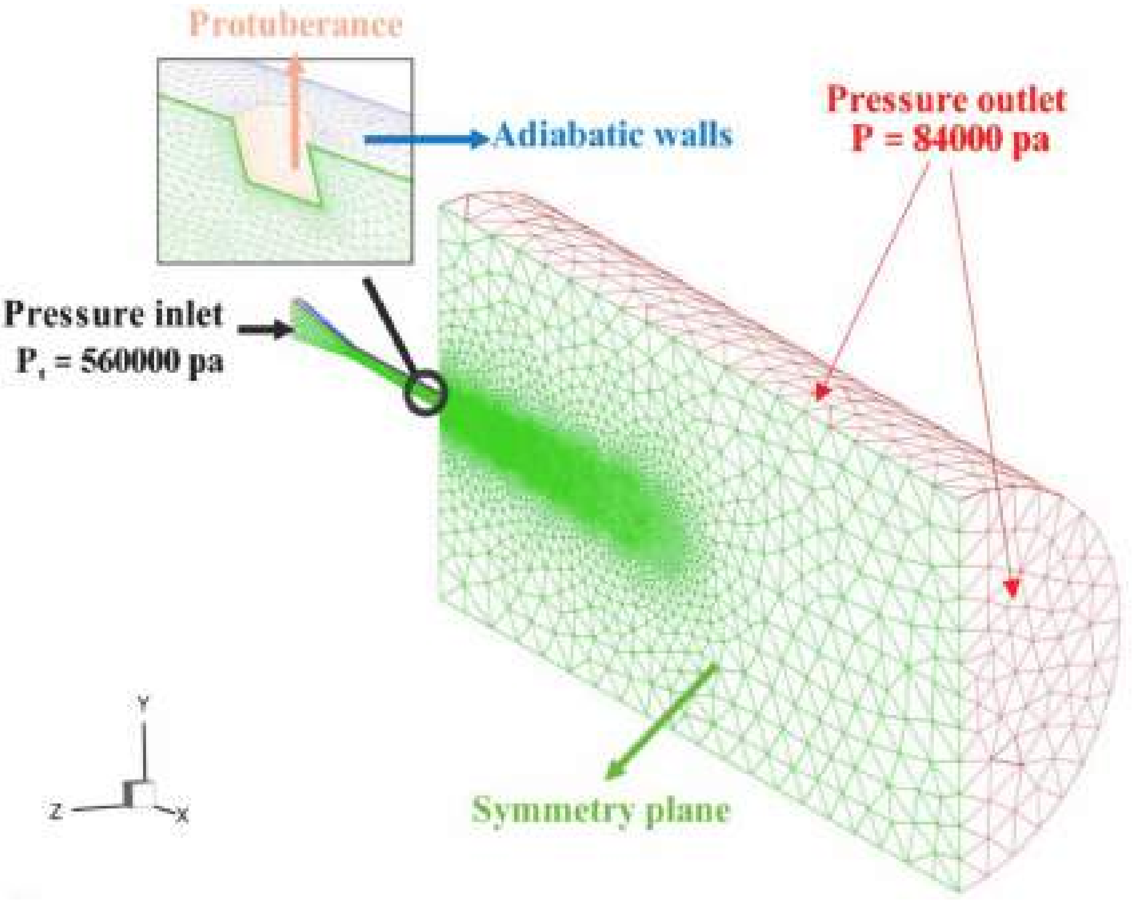

Fig. 5. The domain grid and the boundary conditions.

$$G = \begin{bmatrix} \rho v \\ \rho uv - \tau_{yx} \\ \rho vv + P - \tau_{yy} \\ \rho wv - \tau_{yz} \\ v\left[\rho\left(e + \frac{V^2}{2}\right) + P\right] - u\tau_{yx} - v\tau_{yy} - w\tau_{yz} - q_y \end{bmatrix} \tag{4}$$

$$H = \begin{bmatrix} \rho w \\ \rho uw - \tau_{zx} \\ \rho vw - \tau_{zy} \\ \rho ww + P - \tau_{zz} \\ w\left[\rho\left(e + \frac{V^2}{2}\right) + P\right] - u\tau_{zx} - v\tau_{zy} - w\tau_{zz} - q_z \end{bmatrix} \tag{5}$$

Shear stresses and heat fluxes play most important roles in viscous terms so they have to be calculated more accurately by space discretizing in second order.

$$\tau_{xx} = \frac{2}{3}\mu\left(2\frac{\partial u}{\partial x} - \frac{\partial v}{\partial y} - \frac{\partial w}{\partial z}\right) \tag{6}$$

$$\tau_{xy} = \mu\left(\frac{\partial u}{\partial y} + \frac{\partial v}{\partial x}\right) = \tau_{yx} \tag{7}$$

$$q_x = -k\frac{\partial T}{\partial x} \tag{8}$$

The flow is considered to be compressible, so it is necessary to utilize the equation of state:

$$P = \rho RT = (\gamma - 1)\rho e \tag{9}$$

$$T = \frac{(\gamma - 1)e}{R} \tag{10}$$

The viscosity (kg/(s·m)) is computed based on Sutherland formula as in Eq. [15]:

$$\frac{\mu}{\mu_\infty} = \frac{T_\infty + 110.4}{T + 110.4}\left(\frac{T}{T_\infty}\right)^{\frac{3}{2}} \tag{11}$$

where, U is general (scalar) flow variable, u, v, and w are cartesian velocity components, ρ is density, P is pressure, T is temperature, μ is dynamic viscosity coefficient, τ_{ij} is components of viscous stress tensor, and e is the total specific energy [2,15,46].

The shear-stress transport was used to analyze boundary layer separation, shock generation, and vortex areas in detail. [47–49] The SST k-ω model includes all the refinements of the BSL (Baseline) model and, in addition, accounts for the transport of the turbulence shear stress in the definition of the turbulent viscosity. The SST k-ω transport equations are as follows:

$$\frac{\partial}{\partial t}(\rho k) + \frac{\partial}{\partial x_i}(\rho k u_i) = \frac{\partial}{\partial x_j}\left(\Gamma_k \frac{\partial k}{\partial x_j}\right) + \widetilde{G}_k - Y_k + S_k \tag{12}$$

$$\frac{\partial}{\partial t}(\rho \omega) + \frac{\partial}{\partial x_i}(\rho \omega u_i) = \frac{\partial}{\partial x_j}\left(\Gamma_\omega \frac{\partial \omega}{\partial x_j}\right) + \widetilde{G}_\omega - Y_\omega + D_\omega + S_\omega \tag{13}$$

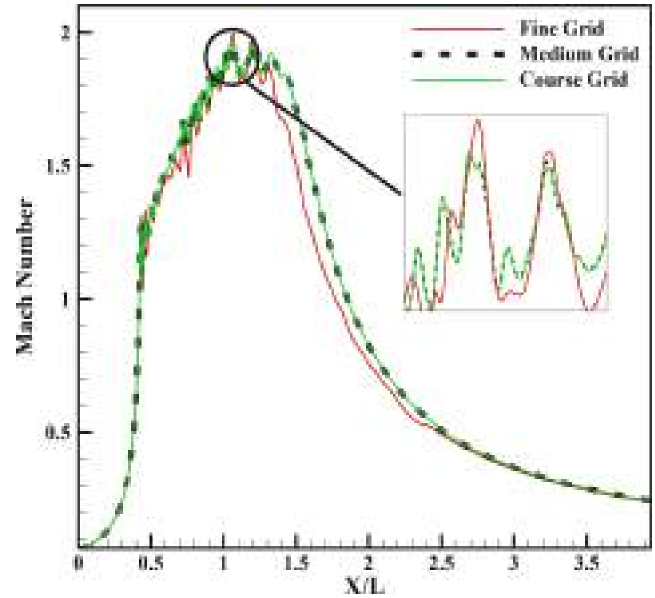

Fig. 6. Variations in the mean vertex average Mach number on the center line of the nozzle for different grids.

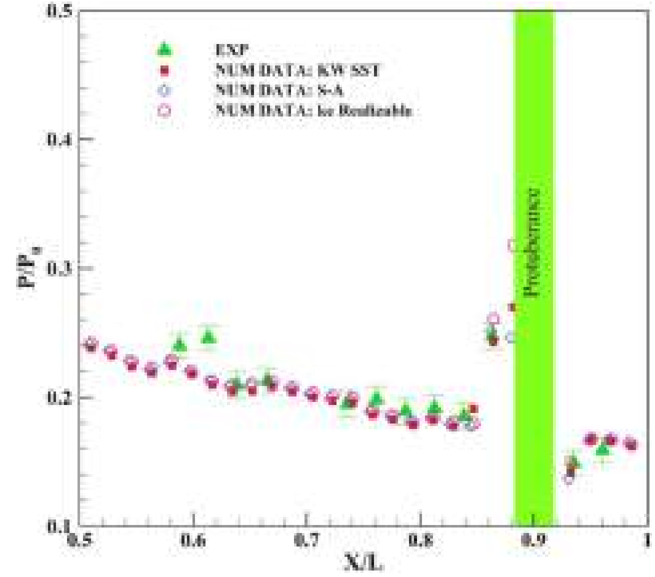

Fig. 7. Comparison of several well-known turbulence models in obtaining the pressure distribution on the nozzle wall.

where; $\widetilde{G}_k$ represent the generation of turbulent kinetic energy due to mean velocity gradient, $\widetilde{G}_\omega$ represent the generation of ω. Γ_k and Γ_ω are effective diffusivity of k and ω, respectively. Y_k and Y_ω represent dissipation of k and ω due to turbulence and, D_ω cross-diffusion term. S_k and S_ω are viscous dissipation terms [2,15].

2.2. Assessment parameters

The thrust deflection angle obtained from the ratio of axial and lateral thrust components (Fx, Fy) is as follows:

$$\alpha = tan^{-1}(Fy/Fx) \tag{14}$$

In the above relation, Fx and Fy are calculated from the flow field parameters extracted from the nozzle exit plane as the following relation:

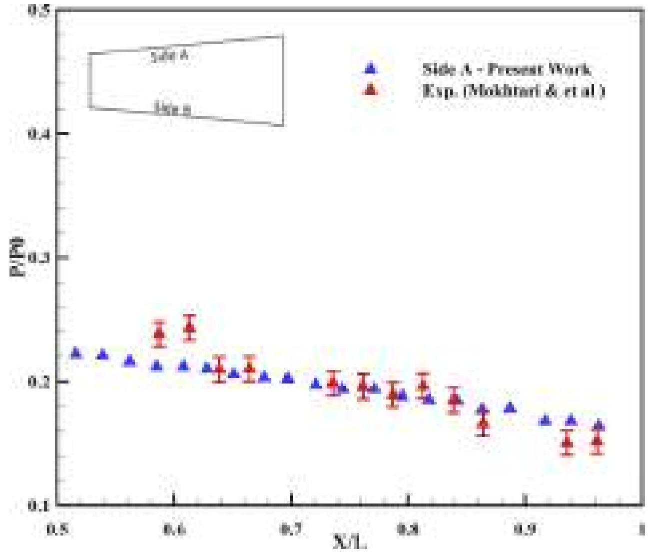

Fig. 8. Comparison of present numerical and experimental results of wall pressure distribution (without protuberance).

$$F_x = (m^{\cdot})V_{ex} + (P_e - P_{atm})A_e \tag{15}$$

$$F_y = (m^{\cdot})V_{ey} \tag{16}$$

Where, V_{ex} and V_{ey} are the exit velocity components, and A_e represents the exit area of the nozzle. In addition, $m^{\cdot}$ is the mass flow rate of the mainstream and P_e, P_{atm} are the nozzle exit plane's pressure and ambient pressure [15].

The existence of a protuberance within the flow path creates an obstruction, leading to shock formation and resulting in a reduction of thrust force. To quantify this loss, the efficiency parameter is defined as follows:

$$\eta = \frac{F_{t\text{with protuberance}}}{F_{t\text{without protuberance}}} \tag{17}$$

Where F_t is the total force obtained from the following relation:

$$F_t = \sqrt{{F_x}^2 + {F_y}^2} \tag{18}$$

2.3. Geometric characteristics and boundary conditions

In this research, a 3-D axisymmetric nozzle based on the dimensions of the reference nozzle [31] and a far-field domain has been considered to simulate nozzle exit flow into the atmosphere. The throat diameter (D^*) is 5 mm, the convergent part of the nozzle length is $7D^*$, and the nozzle exit area is 33.16 mm. The overall nozzle's length is $17D^*$. The width and length of the computational domain at the nozzle exit are 20 and 60 times the diameter of the nozzle throat, respectively. The protuberance is located at 80 %, 85 %, and 95 % of the length of the divergent part of the C-D nozzle. In addition, the height of the protuberance varies from 0.2 to 2 mm.

No slip and adiabatic boundary conditions were used for the nozzle's walls. In all simulations, the stagnation temperature is constant at the nozzle inlet and set at 298.5 K. Also, the stagnation pressure is set so that the NPR varies from 5 to 8. The static pressure is 0.84 bar at the outlet boundaries. The boundary conditions are shown in Fig. 5.

2.4. Grid study

An unstructured grid is used to mesh the computational domain (Fig. 5), with refinement near the walls to capture sharp flow variations

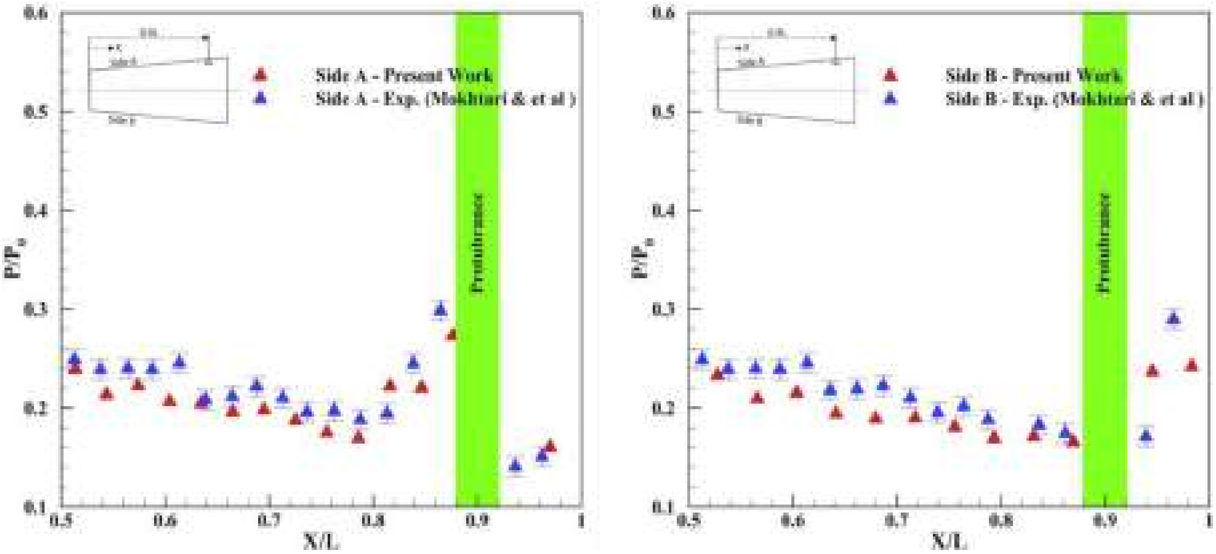

Fig. 9. Comparison of numerical and experimental results of wall pressure distribution ($\frac{H}{D^*}$ = 0.2, and NPR = 6.67).

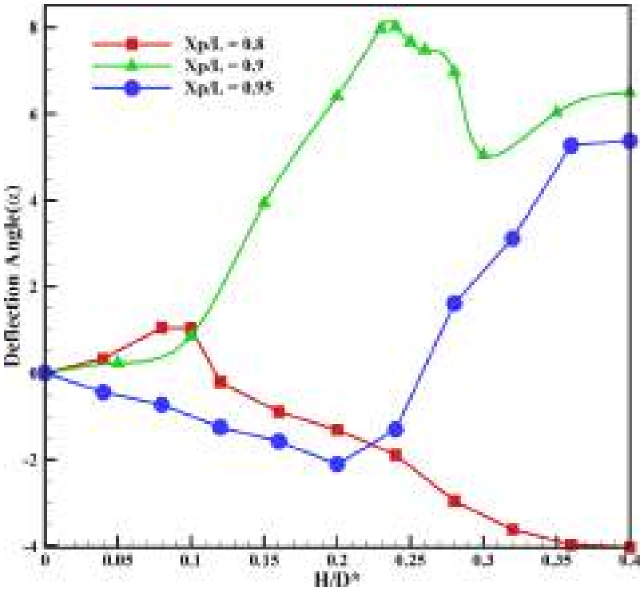

Fig. 10. Thrust deflection angle versus different PPRs.

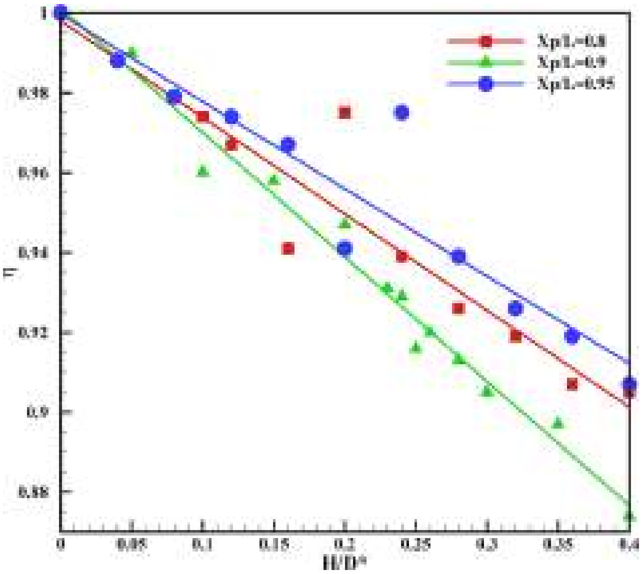

Fig. 11. The nozzle efficiency versus different PPRs.

in the boundary layer. The grid is also refined around the protuberance inside the nozzle to resolve shocks and viscous shear layers accurately. The boundary layer comprises eight cells with a growth factor of 1.1, and the first grid height is on the order of, ensuring precise resolution of abrupt flow changes while maintaining a y^+ value below 1.

The computational domain is discretized using three grid resolutions: 300,000, 600,000, and 1,000,000 elements. Fig. 6 presents the mean vertex average Mach number along the nozzle centerline for different grids. The results show negligible Mach number variations between the medium (600,000) and fine (1,000,000) grids, with identical shock locations. Therefore, the medium grid is selected for further simulations to balance accuracy and computational cost.

To ensure numerical stability, the Courant-Friedrichs-Lewy (CFL) number was initially set to 0.2 until convergence was achieved. Additionally, convergence was confirmed by monitoring the scaled residuals for continuity, momentum, and energy equations, which reached a threshold of 10^{-3}.

3. Results and Discussion

This research has performed a numerical study of TVC in a convergent-divergent nozzle using a protuberance. The parameters studied in this research include NPR, penetration ratio, and protuberance position.

3.1. Validation

For evaluating the numerical results, the pressure distribution on the nozzle wall in NPR = 6.67 is compared with the experimental results [31]. The results show a good agreement between experimental and numerical data. Some minor differences are due to the assumptions used in the numerical solution. The following assumes that a protuberance is in the position $\frac{X_p}{L} = 0.9$, and the pressure on the wall is calculated numerically in the NPR = 6.67. A comparison between the present results and the experimental results [31] is shown in Fig. 7, Fig. 8, and Fig. 9. In this case, a good agreement is observed. A high and low pressure upstream and downstream of the protuberance is observed. The

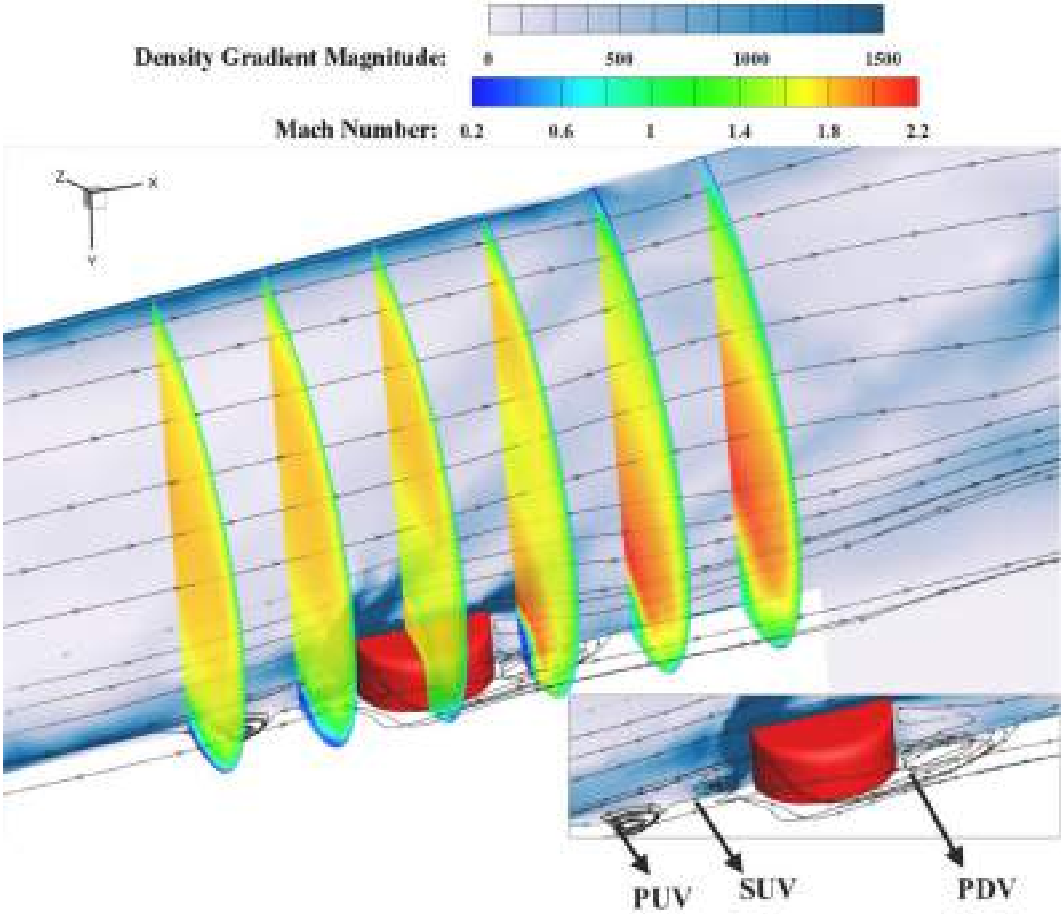

Fig. 12. Mach number and density gradient Magnitude slices in the nozzle divergence at. $NPR = 6.67, \frac{H}{D^*} = 0.15, \frac{X_p}{L} = 0.9$.

leading cause of the discrepancy between the results is the flow turbulence modeling, which has been reported in similar results. In this study, Side A denotes the bottom wall, which the protuberance penetrated, while Side B corresponds to the upper wall, representing the opposite side that incorporates the protuberance.

Fig. 7 presents the pressure distribution on the nozzle wall using three turbulence models: Spalart-Allmaras (SA), SST k-ω, and k-ε Realizable. The results are largely similar, with slight variations near the protuberance. Experimental data indicate that the SST k-ω model provides the most accurate predictions, making it the preferred choice for this study.

Due to its modified eddy viscosity formulation, SST k-ω outperforms the other models in predicting adverse pressure gradients and shockwave-boundary layer interactions. It applies the k-ω model in the sublayer and logarithmic regions while transitioning to k-ε in the wake region and free-shear layers. This model is the only two-equation approach capable of accurately capturing pressure-induced separation and viscous-inviscid interactions [48]. Minor numerical-experimental discrepancies likely arise from averaging and rounding errors. Additionally, Liou et al. found that SST k-ω can predict boundary layer separation earlier than other models in some cases [50].

3.2. Evaluation of the protuberance position effects and flow physics

For investigating the protuberance position effects, it was installed in $\frac{X_p}{L} = 0.8,\ 0.9\ \&\ 0.95,$ and 0.95, and its effects on the thrust vector were investigated. Also, in each case, the protuberance penetration ratio (PPR) $\left(\frac{H}{D^*}\right)$ has changed from 0 to 0.4. The NPR is set to 6.67 in all cases.

Fig. 10 shows the deflection angle of the thrust vector in three investigated positions. These results indicate that when the protuberance is installed in the position $\frac{X_p}{L} = 0.9$ by increasing the penetration ratio up to $\frac{H}{D^*} = 0.24$, the thrust vector angle will increase to 8.01 degrees, and a further increase in the penetration ratio will adversely affect the thrust vector. In other words, by increasing the $\frac{H}{D^*}$ from 0.24, a non-linear behavior is observed in the deflection angle. In other positions of the protuberance, the range of changes in the deflection angle is much lower. Also, a nonuniform increase or decrease trend is observed in the thrust vector angle changes. However, unlike in the first case, after the turning point, the trend of changes in the last two cases is almost linear.

The nozzle thrust vector efficiency is shown in Fig. 11. Results indicate that by increasing the protuberance penetration, the loss of the thrust vector increases linearly in almost all cases. Also, the most significant drop is related to the case where the protuberance is in position $\frac{X_p}{L} = 0.9$. It should be noted that in conditions where the nozzle has the highest deflection angle ($\frac{H}{D^*} = 0.24$, $\frac{X_p}{L} = 0.9$), the rate of thrust loss has increased to nearly 7.5 %.

The flow field at the nozzle exit has been investigated to understand the flow physics better. For this purpose, the flow field of the computational domain is shown in Fig. 12, while NPR, $\frac{X_p}{L}$ and $\frac{H}{D^*}$ are set 6.67, 0.9, and 0.15 respectively. Fig. 12 shows the density gradient contours on the nozzle symmetry plane and the Mach number contours on different cross-sections.

Density gradient contours show that the protuberance significantly affects the nozzle flow field. Also, severe density changes occur upstream and downstream of the protuberance, indicating that two sets of strong shocks have formed upstream and downstream. The shocks

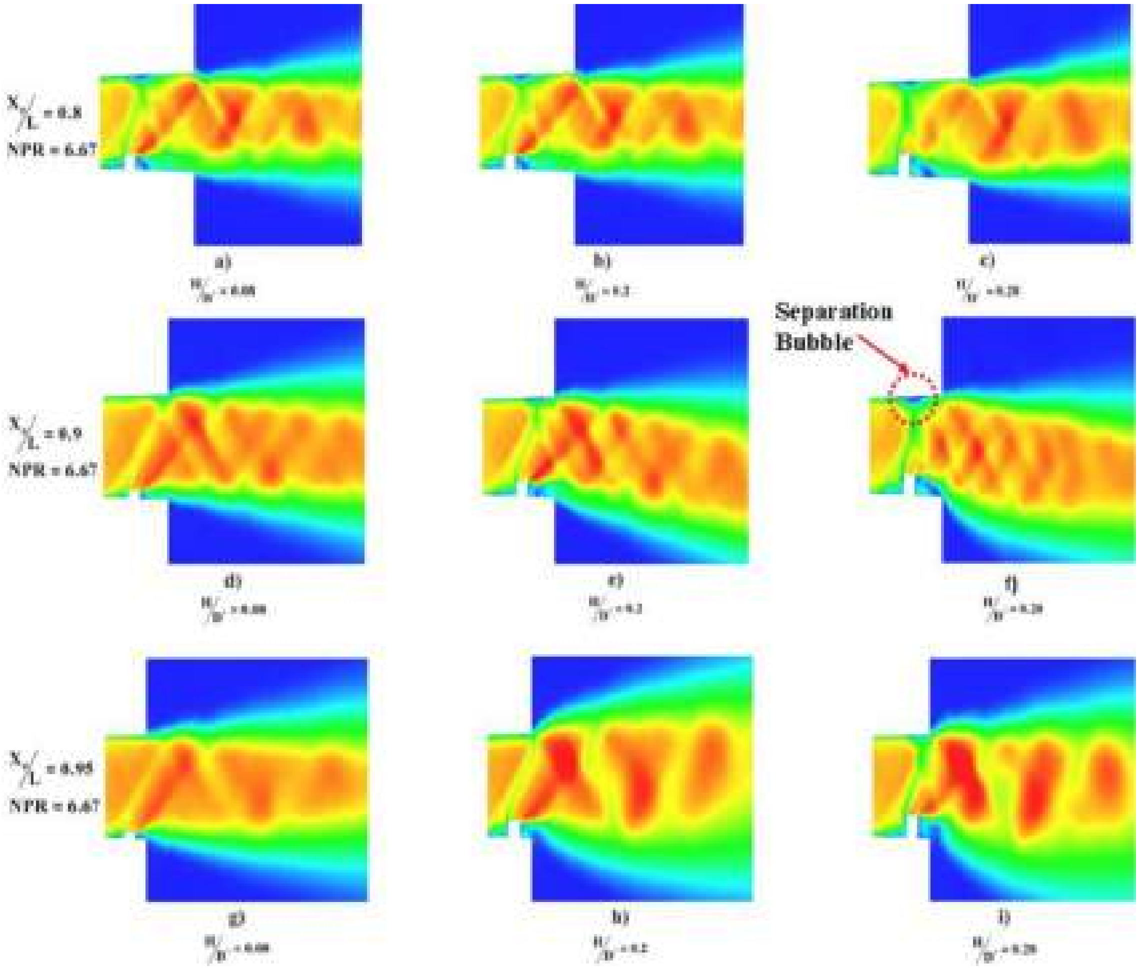

Fig. 13. Mach number counters in the nozzle outlet at NPR = 6.67, H/D*; a, d and g are 0.08, b, e, and h are 0.2, and c, f, and I are 0.28.

formed upstream of the protuberance consist of two separate shocks. The first shock is a bow shock due to the blockage effects of the protuberance, and the second shock is due to the change in the flow direction at the edge of the protuberance. These two shock waves combine to form a stronger wave (λ-lambda shock). The shock is reflected after hitting the opposite wall and exiting the nozzle. The protuberance in the flow field has caused the formation of horseshoe vortices upstream of the protuberance in the area between the two shocks. Also, due to the blockage effects of the protuberance, a wake region is formed downstream of the protuberance where the flow velocity is low. The Mach number contours presented in the cross-section planes of Fig. 12 downstream of the protuberance show that, by moving away from the protuberance, the height of this region gradually decreases. This phenomenon has caused the expansion waves to form above the wake region and increase the flow Mach number. Subsequently, due to the wake area's fixed height, the direction of the supersonic flow passing above this area has changed, and an oblique shock is formed.

By following the flow streamlines at the end of the nozzle, it is observed that the reflected shocks from the opposite wall and its intersection with the shock formed on the wake are the main factors affecting the final direction of the nozzle exit flow. The Mach number contours of the nozzle exit flow are shown in Fig. 13. These contours are presented for different penetration ratios and installed positions of the protuberance. It is revealed that the type of λ-shock reflection from the opposite wall has changed from regular to irregular by increasing protuberance height.

Building upon what is revealed from the flow physics in the presented contours, the primary reason for the non-linear behavior in Fig. 10 is the complex interaction between shock waves and the boundary layer. A strong 3D jet-induced undetached bow shock and a weak separation shock above the protuberance location merge at the triple point, forming a strong incident shock (first λ-shock system). This shock impinges on the opposite wall boundary layer, leading to a shock-wave/boundary-layer interaction and inducing shock-induced separation due to the strong adverse pressure gradient (Fig. 13-a, b, c) [51]. As a result, a separation bubble is formed, as also indicated in the figure. As shown in Fig. 13 (a–c), the size of this bubble at the location of 0.8 and under the investigated pressure ratio is independent of the penetration depth of the protuberance. A comparison of Fig. 13 (d–f) reveals that with an increase in penetration depth at this specific protuberance location and an NPR of 6.67, the separation bubble enlarges and behaves physically like an obstacle. Consequently, it manifests as a secondary protuberance on the opposite wall, thereby reducing the thrust vector deviation as the penetration depth increases.

Another key is stronger interactions are required in turbulent flows to induce separation. In this case, the interaction was sufficient to create a separation bubble, visible as a hump in the supersonic upstream flow (Fig. 13-a, b, c). The thickening of the boundary layer generates weak compression waves ahead of the incident shock, forming a second λ-shock system. Furthermore, when a shock wave's inclination angle is large enough, a regular reflected shock cannot straighten the flow parallel to the wall. Instead, the incident shock reflects on itself, producing a curved, strong shock wave known as Edney Type II interaction (Mach reflection), which propagates almost perpendicular to the wall [52,53].

The thrust vector's final angle depends on the upstream shock reflection type when the protuberance is installed in position $\frac{X_p}{L} = 0.9$.

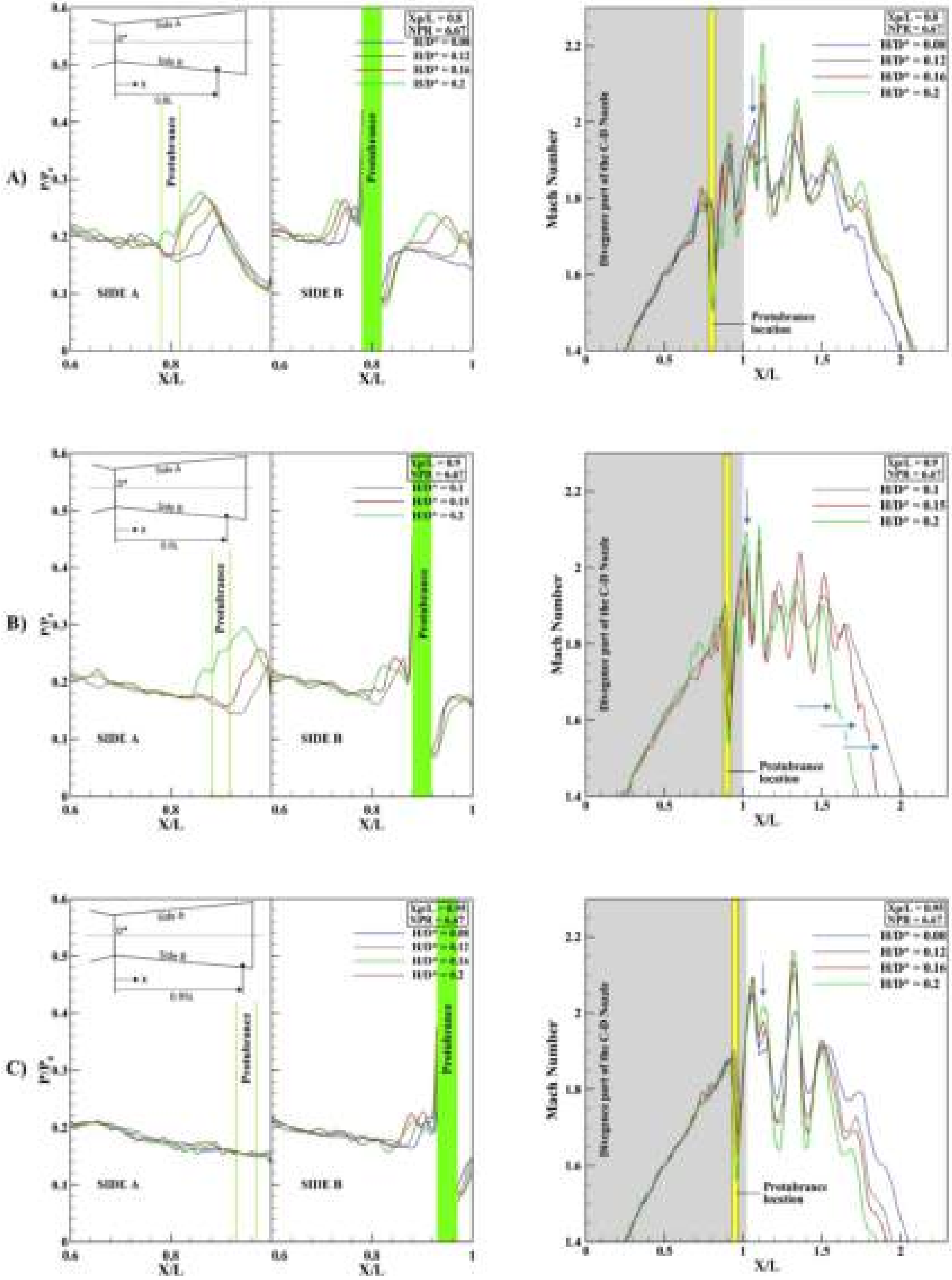

Fig. 14. Investigation of the effects of protuberance penetration on wall pressure distribution and Mach number along the line of symmetry; A) $\frac{X_p}{L} = 0.8$ B)$\frac{X_p}{L} = 0.9$ C).$\frac{X_p}{L} = 0.95$

Also, increasing the Mach number of the flow above the wake region at the higher penetration ratios intensifies the thrust deflection angle Fig. 13 e-f. The Mach disk width increases because the protuberance penetration has increased from the state of the maximum thrust deflection angle Fig. 13 e. Further, due to the enlargement of the Mach disk and its impact on the high-velocity region above the wake, the effects of this region are reduced, and consequently, the thrust deflection angle also decays. The aforementioned behavior can be seen when the protuberance is installed in the position $\frac{X_p}{L} = 0.8$. The difference between the two earlier cases is that the width of the wake region area in the second case has decreased compared to the first case ($\frac{X_p}{L} = 0.9$). This phenomenon causes the shock created in the upper part of the wake to become stronger. Also, this phenomenon has reduced the total flow

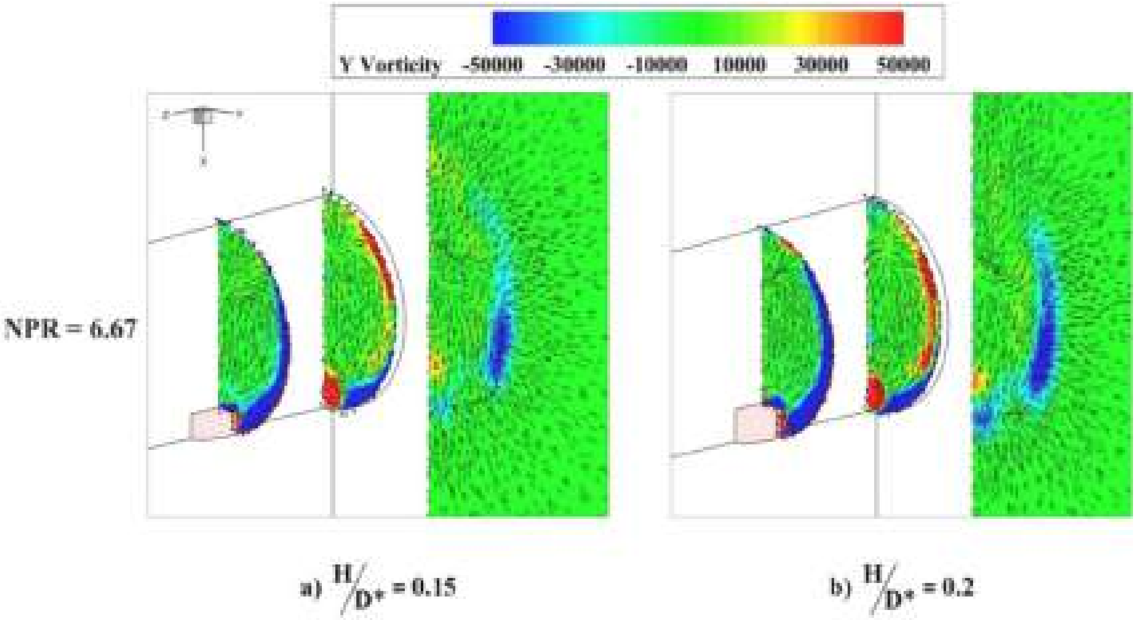

Fig. 15. Development of X-Y component of vorticity field at the different Z/L cross-sections at NPR = 6.67.

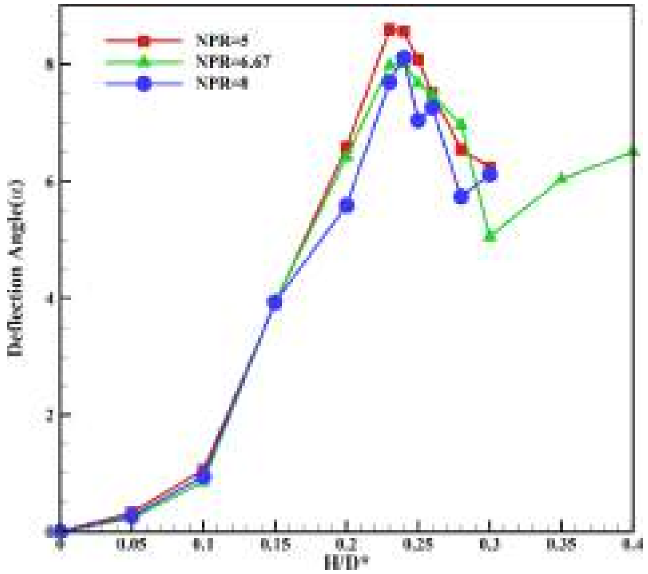

Fig. 16. Rate of deflection at position $\frac{X_p}{L} = 0.9$ and NPR = 5, 6.67 and 8.

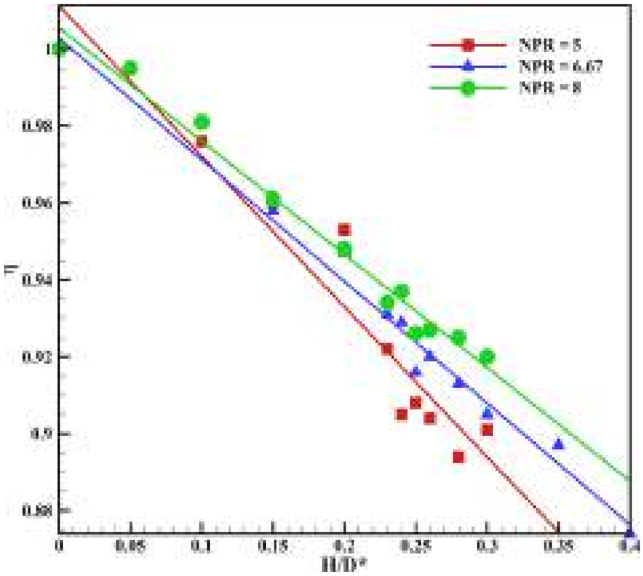

Fig. 17. Efficiency at $\frac{X_p}{L} = 0.9$ and NPR = 5, 6.67 and 8.

deviation at the nozzle output when the protuberance is installed in the position $\frac{X_p}{L} = 0.95$. In a low protuberance penetration ratio (PPR), the upstream shock reflection is not observed in the Mach contours Fig. 13. By increasing the protuberance penetration, the direction of the output flow is gradually reversed due to the upward movement of the upstream shock into the nozzle and hitting the opposite wall.

To investigate the effects of increasing the protuberance penetration on the structure of shocks formed in the flow field, the pressure distribution on the nozzle wall and Mach number changes along the nozzle centerline in different conditions are extracted in Fig. 14. These results show that in all three installation locations of the protuberance, the location of the upstream shock has moved to the inside of the nozzle by increasing the protuberance penetration.

Also, the reflected shock has become stronger by increasing the amount of penetration and moving upwards. However, the increase in the strength of the shocks created by the Mach number changes along the centerline of Fig. 14 is well observed. In Fig. 14, the Mach number changes due to the increase in the penetration ratio have increased. However, in the $\frac{X_p}{L} = 0.95$, shock reflection effects on the opposite wall are not observed. Pressure changes downstream of the protuberance indicate that the width of the wake area increased slightly. However, the pressure in this area has decreased significantly with the increase in PPR. Another point that can be seen from the Mach number changes along the centerline of the nozzle is that the main factor for the thrust vector is the rate of increase in velocity (first peak) at the nozzle output. In addition, changes in Mach number downstream of protuberance indicate that the flow characteristics in this area play a significant role in the final flow path.

Fig. 15 illustrates the development of the X-Y component of the vorticity field at different Z/L cross-sections downstream of the protuberance installation location. These results are presented for two penetration ratios, H/D* = 0.15 and 0.2, at NPR = 6.67. The data reveal that

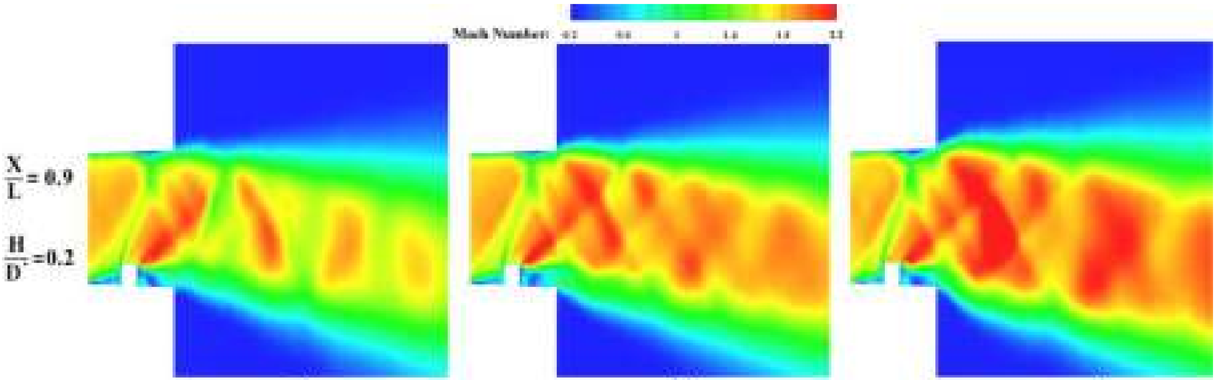

a)
NPR = 5

b)
NPR = 6.67

c)
NPR = 8

Fig. 18. Mach number contours at different pressure ratios.

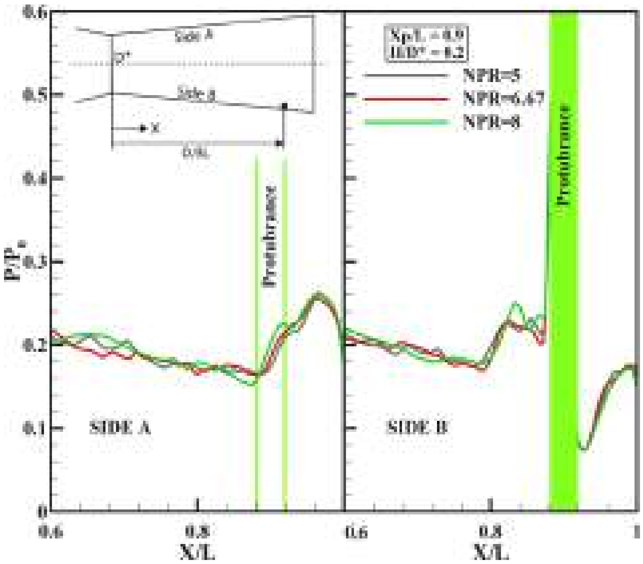

Fig. 19. Investigation of the effects of pressure ratio on the wall.

a vortical flow field forms downstream of the nozzle's protuberance, with vortex strength and width diminishing rapidly outside the nozzle. As the protuberance penetration increases, the vortices grow stronger and more prominent. Notably, in the H/D* = 0.2 case, the vortices are more pronounced and are more likely to interact with downstream fins, leading to jet-fin interactions.

3.3. Evaluation of the NPR effects

The results of the last part showed that in the case where the protuberance is installed in position $\frac{X_p}{L} = 0.9$, the changes in the thrust deflection angle are linear when the height of protuberance increases up to $\frac{H}{D^*} = 0.22$. Unlike other cases, in this case, the difference in the direction of the thrust angle (from positive to negative or vice versa) is not observed by changing the height of protuberance penetration (Fig. 16). Therefore, in this section, in the conditions where the protuberance is installed in the position $\frac{X_p}{L} = 0.9$, the nozzle effects of NPR in the range of 5 to 8 have been investigated. Fig. 16 shows the changes in thrust deflection angle versus the protuberance penetration ratio (PPR) at different NPRs. These results show that for penetration ratios up to H/D = 0.15*, the NPR does not significantly influence the thrust deflection angle. However, for H/D > 0.15*, the deflection angle becomes increasingly dependent on protuberance position and other parameters. Of course, by increasing NPR, the maximum deflection angle decreased slightly, but still, the highest rate of deflection of the thrust vector occurred between $\frac{H}{D^*} = 0.21$ and 0.23*, beyond which a downward trend is observed across all NPR values.

Another point is the sharp decrease in the deflection angle of the thrust vector in PPR greater than $\frac{H}{D^*} = 0.22$, which is observed in all NPRs. Fig. 17 shows the effects of NPR on nozzle efficiency (thrust losses). These results indicate that, generally, the thrust losses increase by increasing NPR to nearly 12 % at the maximum examined protuberance penetration ($\frac{H}{D^*} = 0.4$). However, the linear and decreasing behavior of the nozzle efficiency in all NPRs can be seen by increasing the PPR. The main difference in performance in different NPRs is related to the condition that $\frac{H}{D^*} > 0.22$, and the thrust deflection angle is reduced in these conditions. In other words, in situations where $\frac{H}{D^*} < 0.22$, the thrust loss is less than 5 % and is not significantly affected by NPR.

Fig. 18 shows the Mach number contours in three different NPRs to better understand NPR effects on the flow field. while $\frac{H}{D^*} = 0.2$, and the protuberance location is $\frac{X_p}{L} = 0.9$. These results show that despite the sharp changes in the Mach number contours downstream of the protuberance at different NPRs, the overall flow direction has not changed significantly. However, observing the structure of the waves downstream of the protuberance, it can be seen that by increasing NPR, these structures have not changed, and only due to the increase in output flow pressure will more stronger shock and expansion waves be formed. Furthermore, the rise in NPR did not significantly affect the oblique shock formed upstream of the protuberance and its position. Therefore, it has caused other phenomena that have formed downstream, and even the protuberance wake area does not change significantly. This can also be seen in the pressure changes on the nozzle walls shown in Fig. 19. However, these results show that the increase in NPR causes the upstream shock point of the protuberance to move downwards a little, and its strength is slightly increased. In addition, the primary upstream vortex (PUV) strength increases when NPR increases.

4. Conclusion

This study numerically investigated the effects of installing a cylindrical protuberance in the divergent section of a supersonic nozzle with a nominal Mach number of 2. The impact of protuberance position and penetration ratio was analyzed under over-expanded and under-expanded nozzle conditions. The compressible Navier-Stokes equations were solved using the SST k-ω turbulence model to capture Reynolds stresses. The numerical results showed good agreement with previous experimental data, confirming the model's accuracy.

Key findings include:

- The optimal protuberance position was $\frac{X_p}{L} = 0.9$, where the thrust deflection angle reached 8.1° at a penetration ratio of 0.22. Under these conditions, a linear relationship was observed between penetration ratio and deflection angle.
- At $\frac{X_p}{L} = 0.9$, increasing the NPR reduced the maximum deflection angle by approximately 5 %. However, the highest thrust vector deviation consistently occurred near a penetration ratio of 0.22.
- Thrust vector loss increased linearly with penetration depth. At $\frac{X_p}{L} = 0.9$ and $H/D = 0.22$, the system experienced the highest thrust vector losses, reaching 6.5 %.
- Increasing NPR had minimal effect on nozzle performance at $H/D = 0.22$ (maximum deflection angle). However, for $H/D > 0.22$, nozzle performance improved under under-expanded conditions.

These simulations complemented experimental results by providing detailed insights into shock-shock interactions and the far field's vortex dynamics. This study's comprehensive numerical dataset also serves as a benchmark for future aerospace research. The findings offer valuable guidance for designing advanced propulsion systems with enhanced thrust vectoring control across various operating conditions.

CRediT authorship contribution statement

Mohammad Hojaji: Supervision, Methodology, Formal analysis. **Mohammad Eydizadeh:** Investigation, Validation. **Mohammadreza Soufivand:** Writing – review & editing. **Annunziata D'Orazio:** Writing – review & editing. **Sayed Ali Hosseini:** Writing – review & editing. **Arash Karimipour:** Writing – review & editing. **Aliakbar Karimipour:** Writing – review & editing.

Declaration of competing interest

The authors declare that they have no known competing financial interests or personal relationships that could have appeared to influence the work reported in this paper.

References

[1] Noaman H, Tang HB, Khalil E. Numerical simulation on the influence of injection location, injection angle, and divergence half angle on SITVC nozzle flow field. Int J Aerospace Eng 2019;2019:7392497.
[2] Wu K, Kim TH, Kim HD. Theoretical and numerical analyses of aerodynamic characteristics on shock vector control. J Aerosp Eng 2020;33:04020050.
[3] Wu K, Zhang G, Kim TH, Kim HD. Numerical parametric study on three-dimensional rectangular counter-flow thrust vectoring control. Proc Inst Mech Eng, G: J Aerospace Eng 2020;234:2221–47.
[4] D.J. Wing, V.J. Giuliano, Fluidic thrust vectoring of an axisymmetric exhaust nozzle at static conditions, in: 1997 ASME Fluids Engineering Division Summer Meeting (FEDSM''97), 1997.
[5] R.D. Guhse, An experimental investigation of thrust vector control by secondary injection, in, 1965.
[6] R. Dhinagaran, T. Bose, Comparison of Euler and Navier-Stokes solutions for nozzle flows with secondary injection, In: 34th aerospace sciences meeting and exhibit, 1996, pp. 453.
[7] Lee S-H. Characteristics of dual transverse injection in scramjet combustor, part 1: Mixing. J Propul Power 2006;22:1012–9.
[8] Wu K, Dong Kim H. Numerical study on the shock vector control in a rectangular supersonic nozzle. Proc Inst Mech Eng, G: J Aerospace Eng 2019;233:4943–65.
[9] Hojaji M, Razavi Dehkordi SMH, Hosseini SA, Pourmohammadi M, Norouzi M. Experimental investigation of the effects of secondary flow injection on the output flow of the convergent-divergent nozzle at different beveled angles. J Aeronautical Eng 2022;24:45–56.
[10] Tahani M, Hojaji M, Salehifar M, Dartoomian A. Numerical investigation of sonic jet injection effects on flow field structure and thrust vector control performance in a supersonic nozzle. Modares Mech Eng 2015;15.
[11] Shin CS, Kim HD, Setoguchi T, Matsuo S. A computational study of thrust vectoring control using dual throat nozzle. J Therm Sci 2010;19:486–90.
[12] Deng R, Kong F, Kim HD. Numerical simulation of fluidic thrust vectoring in an axisymmetric supersonic nozzle. J Mech Sci Technol 2014;28:4979–87.
[13] Deng R, Setoguchi T, Kim HD. Large eddy simulation of shock vector control using bypass flow passage. Int J Heat Fluid Flow 2016;62:474–81.
[14] Zmijanovic V, Lago V, Palerm S, Oswald J, Sellam M, Chpoun A. Thrust shock vector control of an axisymmetric CD nozzle via transverse gas injection. In: 28th International Symposium on Shock Waves: Vol 2. Springer; 2012. p. 171–7.
[15] Salehifar M, Tahani M, Hojaji M, Dartoomian A. CFD modeling for flow field characterization and performance analysis of HGITVC. Appl Therm Eng 2016;103:291–304.
[16] Wu K, Kim T, Kim H. Numerical study of fluidic thrust vector control using dual throat nozzle. J Appl Fluid Mech 2020;14:73–87.
[17] Zigunov F, Sellappan P, Alvi FS. Reduction of noise in cold and hot supersonic jets using active flow control guided by a genetic algorithm. J Fluid Mech 2022;952:A40.
[18] Zigunov F, Song M, Sellappan P, Alvi FS. Multiaxis shock vectoring control of overexpanded supersonic jet using a genetic algorithm. J Propul Power 2023;39:249–57.
[19] Kim H, Han D-H, Lee TH, Hong J-W. An application of machine learning for geometric optimization of a dual-throat bent nozzle. Adv Eng Softw 2025;202:103869.
[20] S.A. Hosseini, E. Goshtasbi-Rad, M. Hojaji, Experimental and Numerical Investigation of the Effect of Secondary Flow Injection on the Thrust Vector Control of Supersonic C-D Beveled Nozzles, Available at SSRN 5125591.
[21] Sutton GP, Biblarz O. Rocket propulsion elements. John Wiley & Sons; 2016.
[22] Carpenter TW, Vaccarezza SE, Dobbins S. Design and evaluation of single and dual flow thrust vector nozzles with post exit vanes. Semiannual Prog Rep 1992.
[23] Mokhtari D. Experimental study of effect of obstacle presence and its geometry on thrust vector and outlet jet in a convergent-divergent micro nozzle. Modares Mech Eng 2020;20:1211–21.
[24] Babaeyan M, Hojaji M. Experimental investigation of the penetration effects of opposite dual protuberances on thrust vector of a supersonic C-D nozzle. Modares Mech Eng 2019;19:1741–50.
[25] Babaeyan MR. Experimental investigation of the influence of transverse dual protuberances on the thrust vector of a supersonic C-D nozzle. J Appl Comput Sci Mech 2020;31:139–54.
[26] Shah K, Abdeljawad T. On complex fractal-fractional order mathematical modeling of CO_2 emanations from energy sector. Phys Scr 2023;99:015226.
[27] Shah K, Amin R, Abdeljawad T. Utilization of Haar wavelet collocation technique for fractal-fractional order problem. Heliyon 2023;9.
[28] Phanindra BC, Rathakrishnan E. Corrugated tabs for supersonic jet control. AIAA J 2010;48:453–65.
[29] Živković SŽ, Milinović MM, Stefanović PL, Pavlović PB, Gligorijević NI. Experimental and simulation testing of thermal loading in the jet tabs of a thrust vector control system. Therm Sci 2016;20:275–86.
[30] Wu K, Kim T, Kim H. Sensitivity analysis of counterflow thrust vector control with a three-dimensional rectangular nozzle. J Aerosp Eng 2021;34:04020107.
[31] Mokhtari D, Hojaji M, Afrand M. Experimental investigation of the effect of cylindrical protuberance with different penetration the thrust vector a CD nozzle in supersonic regime. Modares Mech Eng 2019;19:1145–54.
[32] Mokhtari D, Hojaji M, Afrand M. Experimental investigation of the effect of location of cylindrical protuberance on the thrust vector of a supersonic CD nozzle. J Solid Fluid Mech 2019;9:237–49.
[33] Mokhtari D, Hojaji M, Afrand M. Numerical/experimental investigation of the presence of a protuberance in a convergent–divergent nozzle in supersonic regime to control the thrust vector. Amirkabir J Mech Eng 2021;53:4887–904.
[34] Babaeyan M, Hojaji M. Experimental investigation of the penetration effects of opposite dual protuberances on thrust vector of a supersonic CD nozzle. Modares Mech Eng 2019;19:1741–50.
[35] Babaeyan MR, Hojaji M. Experimental investigation of the influence of transverse dual protuberances on the thrust vector of a supersonic CD nozzle. J Appl Comput Sci Mech 2020;31:139–54.
[36] Thillaikumar T, Bhale P, Kaushik M. Experimental investigations on the strut controlled thrust vectoring of a supersonic nozzle. J Appl Fluid Mech 2020;13:1223–32.
[37] Soufivand M, Hojaji M, Ghafouri S, D'Orazio A, Siabidzade MA, Karimipour A. Performance evaluation, sensitivity analysis, and mitigating instabilities of Coanda effect-based flow control for a transonic jet: The investigation of shock effects. Ain Shams Engineering Journal 2025;16(6):103381.
[38] Li D, Wu K. Numerical study on rod thrust vector control for physical applications. Int J Aerosp Eng 2021;2021:1–15.
[39] Soufivand MR, Hojaji M, Dehkordi MHR. Protuberance placement mastery: shock wave control integration with Coanda effect to thrust vectoring on a sonic jet. Eng Anal Bound Elem 2024;166:105769.
[40] Tahani M, Hojaji M, Mahmoodi Jezeh SV. Turbulent jet in crossflow analysis with LES approach. Aircr Eng Aerosp Technol 2016;88:717–28.
[41] Hojaji M, Soltani M, Taeibi-Rahni M. New visions in experimental investigations of a supersonic under-expanded jet into a high subsonic crossflow. Proc Inst Mech Eng, G: J Aerosp Eng 2010;224:1069–80.
[42] Viti V, Neel R, Schetz JA. Detailed flow physics of the supersonic jet interaction flow field. Phys Fluids 2009;21.
[43] Gruber M, Nejad A, Chen T, Dutton JC. Mixing and penetration studies of sonic jets in a Mach 2 freestream. J Propul Power 1995;11:315–23.
[44] Zmijanovic V, Lago V, Leger L, Depussay E, Sellam M, Chpoun A. Thrust vectoring effects of a transverse gas injection into a supersonic cross flow of an axisymmetric convergent-divergent nozzle. Prog Propulsion Phys 2013;4:227–56.
[45] Li D, Wu K. Numerical study on rod thrust vector control for physical applications. Int J Aerosp Eng 2021;2021:6963728.
[46] Blazek J. Computational fluid dynamics: principles and applications. Butterworth-Heinemann; 2015.

[47] Menter FR. Improved two-equation k-omega turbulence models for aerodynamic flows. In 1992.

[48] Menter FR. Two-equation eddy-viscosity turbulence models for engineering applications. AIAA J 1994;32:1598–605.

[49] L. Könözsy, The k-ω shear-stress transport (SST) turbulence model, in: A new hypothesis on the anisotropic reynolds stress tensor for turbulent flows: volume i: theoretical background and development of an anisotropic hybrid k-omega shear-stress transport/stochastic turbulence model, Springer, 2019, pp. 57-66.

[50] Liou WW, Huang G, Shih T-H. Turbulence model assessment for shock wave/ turbulent boundary-layer interaction in transonic and supersonic flows. Comput Fluids 2000;29:275–99.

[51] M.A. Saad, Compressible fluid flow, Englewood Cliffs, (1985).

[52] B. Edney, Anomalous heat transfer and pressure distributions on blunt bodies at hypersonic speeds in the presence of an impinging shock, in, 1968, pp. Medium: ED; Size: Pages: 92.

[53] Babinsky H, Harvey JK. Shock wave-boundary-layer interactions. Cambridge University Press; 2011.